Journal of Colloid and Interface Science 490 (2017) 608–620

Contents lists available at ScienceDirect

Journal of Colloid and Interface Science

journal homepage: www.elsevier.com/locate/jcis

Regular Article

Molecular dynamics simulations of cesium adsorption on illite nanoparticles

Laura N. Lammers [a,b,*], Ian C. Bourg [a,c], Masahiko Okumura [d], Kedarnath Kolluri [a], Garrison Sposito [b], Masahiko Machida [d]

[a] Earth and Environmental Sciences Area, Lawrence Berkeley National Laboratory, Berkeley, USA
[b] Department of Environmental Science, Policy, and Management (ESPM), University of California, Berkeley, Berkeley, USA
[c] Department of Civil and Environmental Engineering (CEE) and Princeton Environmental Institute (PEI), Princeton University, Princeton, USA
[d] Center for Computational Science and e-Systems, Japan Atomic Energy Agency, Kashiwa, Japan

GRAPHICAL ABSTRACT

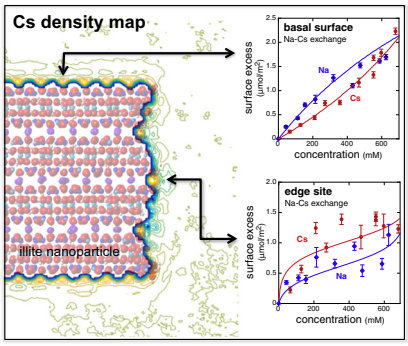

ARTICLE INFO

Article history:
Received 12 August 2016
Revised 21 November 2016
Accepted 23 November 2016
Available online 29 November 2016

Keywords:
Radiocesium
Molecular dynamics simulations
Geochemistry

ABSTRACT

The charged surfaces of micaceous minerals, especially illite, regulate the mobility of the major radioisotopes of Cs (^{134}Cs, ^{135}Cs, ^{137}Cs) in the geosphere. Despite the long history of Cs adsorption studies, the nature of the illite surface sites remains incompletely understood. To address this problem, we present atomistic simulations of Cs competition with Na for three candidate illite adsorption sites – edge, basal plane, and interlayer. Our simulation results are broadly consistent with affinities and selectivities that have been inferred from surface complexation models. Cation exchange on the basal planes is thermodynamically ideal, but exchange on edge surfaces and within interlayers shows complex, thermodynamically non-ideal behavior. The basal planes are weakly Cs-selective, while edges and interlayers have much higher affinity for Cs. The dynamics of Na—Cs exchange are rapid for both cations on the basal planes, but considerably slower for Cs localized on edge surfaces. In addition to new insights into Cs adsorption and exchange with Na on illite, we report the development of a methodology capable of simulating fully-flexible clay mineral nanoparticles with stable edge surfaces using a well-tested interatomic potential model.

* Corresponding author at: Department of Environmental Science, Policy, and Management (ESPM), University of California, Berkeley, Berkeley, USA.
E-mail addresses: lnlammers@berkeley.edu (L.N. Lammers), bourg@princeton.edu (I.C. Bourg), okumura.masahiko@jaea.go.jp (M. Okumura), kedar.kolluri@gmail.com (K. Kolluri), gsposito@berkeley.edu (G. Sposito), machida.masahiko@jaea.go.jp (M. Machida).

http://dx.doi.org/10.1016/j.jcis.2016.11.084
0021-9797/

1. Introduction

Any future reliance on nuclear energy to play a major role in lessening our dependence on fossil fuels brings with it a need to address the potential for long-term environmental contamination by radioisotopes [71]. Two isotopes of cesium, ^{135}Cs and ^{137}Cs, are among the most important contaminants associated with the nuclear fuel cycle because of their high fission yield, long half lives (2.3×10^6 and 30 a, respectively), high solubility in water, and metabolic similarity to potassium. These radioisotopes are key concerns in the geologic storage of radioactive waste [60,35,17], the management of legacy sites contaminated during the development of nuclear power [28,70], and the remediation of soils contaminated by catastrophic releases such as those that occurred at the Chernobyl and Fukushima Daiichi nuclear power plants [31,104,105]. In the Fukushima region, in particular, ^{137}Cs is the main source of external radiation dose five years after the nuclear disaster of March 2011. The most important process controlling the solubility and mobility of cesium in soils, sediments, and sedimentary rocks is the formation of strong surface complexes with clay minerals [1] and particularly with the micaceous minerals, illite, vermiculite, and mica [28,40,11,63,65]. Cesium adsorption on illite is of particular importance in the geologic storage of radioactive waste, because illite often dominates the mineralogy of fine-grained sedimentary rocks considered for use as host formations [94,35,17].

Studies of the adsorption of Cs by illite have a long history [96,83,27,15,22,87,90,74,76,14,61,62,8,106,53,3,25,6,100]. Recent efforts have deployed a combination of wet chemistry experiments [102,4,26], high-resolution imaging [47,63,95,34], synchrotron X-ray spectroscopy [29,42], and atomistic-level simulations [68,93,44,107] to gain detailed insight into Cs adsorption mechanisms, selectivity, and kinetics. The emerging view from these studies is that Cs adsorption involves at least three types of surface sites: *basal sites* located on the external basal surfaces of illite particles, *slow sites* located in anhydrous illite interlayers, and *high affinity sites* of unclear nature. Adsorption on the basal sites is rapid (< 24 h), reversible, and weakly selective (Table 1). The slow sites have slow adsorption and desorption kinetics (likely weeks to months) and a higher total capacity than the basal sites. Finally, the high affinity sites have a very small total capacity and a very high affinity for cesium and other weakly hydrated cations (K^+, NH_4^+). The high-affinity sites and slow sites are particularly important, because they control the long-term migration of cesium in the geosphere [20,100,84].

Despite the importance of the high-affinity and slow sites of illite for cesium fate and transport, important questions remain unanswered regarding the properties of these sites. First, the structure of the high affinity sites is a continuing topic of investigation [46,62,93,68]. The predominant hypothesis is that they occur in "wedge" regions where illite or vermiculite interlayers transition from a collapsed state to an expanded state [18,102,68,107]. The existence of these regions is supported by electron microscopy observations showing that weathering induces a discernible "fraying" at the edges of illite and mica crystals [62,34], perhaps associated with the replacement of K by solvated Ca near the extremities of the anhydrous interlayers [34]. Second, the cation exchange kinetics and selectivity of the slow sites remain poorly understood, in part because of a lack of long-term adsorption and desorption studies. For example, some studies have hypothesized that basal and slow sites have essentially the same Na—Cs exchange selectivity [4], whereas atomistic simulations suggest that Cs is much more selectively retained in anhydrous clay interlayers than on external basal surfaces [79]. The few geochemical modeling studies that described slow sites as distinct surface sites treated them as ideal cation exchangers [22,100] despite evidence that these sites, at least in some cases, form interstratified structures in which Cs displaces K in some interlayers but not in others [69]. Finally, the adsorption-desorption kinetics of the slow and high-affinity sites remain incompletely understood. For example, several studies have shown that solution chemistry strongly affects the kinetics of adsorption on slow sites [4] and desorption from high-affinity sites [25], perhaps through a mechanism analogous to the well known salinity-dependence of smectite clay swelling [86,45]. Geochemical models of cesium adsorption on illite almost invariably ignore the slow sites [14,91,35,33] or assume that their properties are identical to those of the basal sites [4] or the high-affinity sites [100]. The range of values of Na—Cs and K—Cs exchange selectivity coefficients used in surface complexation models is shown in Table 1.

The questions listed above persist in part because the three types of surface sites are challenging to isolate experimentally. For example, spectroscopic or elemental mapping results are challenging to obtain at the very low surface loadings characteristic of the high affinity sites. Atomistic simulation techniques such as molecular dynamics (MD) simulations and density functional theory (DFT) calculations can, in principle, circumvent these difficulties by allowing a direct observation of individual Cs ions on different surface sites. Existing simulation studies have probed cesium adsorption in the interlayer nanopores of swelling clay minerals [64,97,78,79,10,44], in anhydrous clay interlayers [79,93], and at illite and vermiculite wedge sites [68,107]. However, no existing atomistic simulation study has examined cesium adsorption selectivity on different surfaces of a single illite particle, because of two methodological challenges. *Ab initio* MD (*i.e.*, time-dependent DFT) simulations are limited to timescales up to ~100 ps that are significantly shorter than the characteristic timescales of Cs migration on hydrated clay surfaces (on the order of nanoseconds [64,10]). Classical MD simulations can probe timescales up to ~100 ns, but their predictions can be highly sensitive to the choice of inter-atomic potential parameters. The most well-tested inter-atomic potential model for clay-water systems, the CLAYFF model of Cygan et al. [23], was designed to simulate the basal surfaces of infinite clay particles, and its ability to describe the edge surfaces of clay particles is not well established. In fact, even the detailed microstructure and stoichiometry of clay edge surfaces remains poorly constrained [16,9,67].

Here, we present the first ever atomistic simulation study of Cs adsorption on three binding sites (basal, edge, and interlayer) of a model illite nanoparticle. To account for the slow migration of Cs near clay surfaces, our simulations used relatively long (50 ns) classical MD simulations in combination with thermodynamic integration calculations (*i.e.*, alchemical transformations wherein short-range interaction potential parameters for Na are incrementally adjusted to Cs at different sites on the illite surface). In addition to new insights into Cs adsorption on illite, a significant outcome of our study is the development of a methodology capable

Table 1
Cation exchange selectivities of the high affinity and basal sites used in surface complexation models of Cs adsorption on illite and related minerals. Some models also include an intermediate affinity site of unclear mechanistic basis. The table shows the range of values used in existing models of illite surface chemistry [15,74,14,91,54,100,36,17,33,4,29]. For comparison, values for smectite basal surfaces are shown in the last column as calculated by Bourg and Sposito [11] based on previous studies. Cesium exchange selectivity on smectite increases with layer charge (values are reported for smectite layer charges ranging from 0.7 to 1.4 $mol_c\ kg^{-1}$). The notation $K_{eq}^{i/j}$ refers to the equilibrium constant for the replacement of i by j on illite surface sites.

Site type	Illite basal site	Illite high affinity site	Smectite basal site
log $K_{eq}^{Na/Cs}$	1.6–2.0	6.6–7.2	0.7–1.7
log $K_{eq}^{K/Cs}$	0.4–1.1	4.1–5.5	0.2–1.2

of simulating fully-flexible illite nanoparticles with stable edge surfaces based on a well-tested interatomic potential model.

2. Simulation methodology

Atomistic simulations were performed using the molecular dynamics (MD) simulation code LAMMPS, which solves Newton's equations of motion for many-particle systems interacting through pairwise potentials [73]. Interatomic interactions were described as the sum of Coulomb and dispersive (Lennard-Jones 6-12) interactions using the well-known SPC/E water model [5], the CLAYFF model of mineral-water interactions [23], and the Smith-Dang parameters for Na, K, Cs, and Cl [88,24]. Interactions between unlike atoms were derived using the Lorentz-Berthelot combining rules. Our choice of force fields has been successfully tested against experimental data on the structure and dynamics of water and ions on basal surfaces of 2:1 clay minerals [10,30,58,41] and on hydroxylated silica and quartz surfaces [85,13]. In the case of clay-water systems, MD simulation studies have focused almost exclusively on the basal surfaces and hydrous interlayer nanopores. Adsorption on clay edge surfaces remains almost entirely unexamined, in part because the CLAYFF model was not parameterized to simulate clay edge surfaces. The few existing MD simulations of clay edges focused on smectite [78,43,67,99] or pyrophyllite [59,66] rather than illite. Only three of these studies used fully flexible clay structures [59,66,67].

2.1. System setup

A four-layer illite nanoparticle was constructed using the structural parameters reported in Gualtieri [37]. Edge surfaces were created by cleaving the crystal structure along the so-called AC bond chain identified by periodic bond chain theory [103], the most stable or one of the most stable cleavage planes according to quantum mechanical calculations [19,50,49]. Because of the periodic boundary conditions, the resulting nanoparticle is effectively an infinite needle elongated parallel to the crystallographic b-axis and cleaved along the AC plane. Isomorphic substitutions of Si by Al were distributed randomly throughout the particle according to the chemical formula of illite, $K_{0.7}Al_2(Si_{3.3}Al_{0.7})O_{10}(OH)_2$, with the constraint that isomorphic substitutions were not allowed to occur in neighboring tetrahedra [81]. Charge-balancing K ions were initially distributed randomly in ditrigonal cavity positions in the anhydrous interlayers and on external basal surfaces, with the average occupancy of cavity positions being twice as large in the interlayer as on the external surfaces. The initial potassium ion distribution was later optimized as described in Section 2.2. The illite nanoparticle was surrounded by a bath of water molecules and Na, Cs, and Cl ions (total of 33,403 atoms).

As noted above, illite edge surfaces were created by cleaving the illite crystal along the so-called AC bond chain. Then, the cleaved edge surfaces were healed by attaching O atoms to undercoordinated edge metals (Fig. 1). The resulting edge surface carries four distinct types of O atoms: *aluminol* O atoms (Oe3) coordinated to octahedral Al atoms (≡Al_O—O), *bridging* O atoms (Oe6) coordinated to tetrahedral Si and octahedral Al atoms (≡Al_O—O—Si≡), and two types of *silanol* O atoms (Oe1, Oe2) coordinated to tetrahedral Si atoms (≡Si—O). The structure also carries three additional types of surface O atoms resulting from isomorphic substitutions of Si by Al atom near Oe1, Oe2, and Oe6 atoms (referred to as Oe4, Oe5, and Oe7, respectively). Finally, edge O atoms were protonated in accordance with the expected protonation state at near-neutral pH conditions. Specifically, Oe1, Oe2, Oe4, and Oe5 atoms were assigned a single proton, Oe3 atoms were doubly protonated, and Oe6 and Oe7 atoms were not protonated [7,98,9,55]. The resulting edge surface has a net proton surface charge of zero.

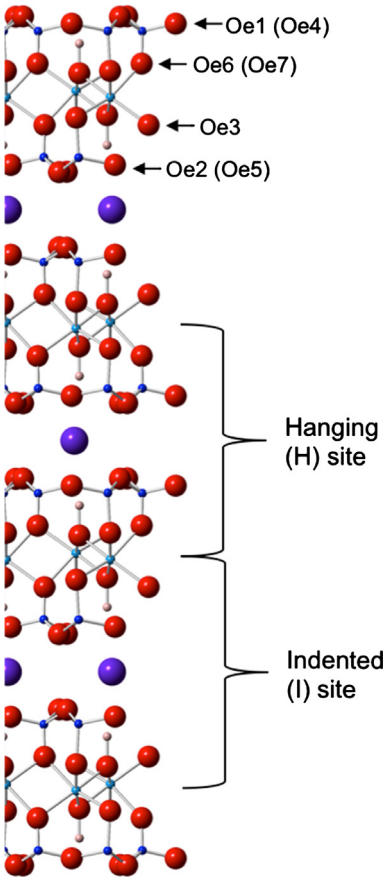

Fig. 1. Schematic view of the illite AC edge surface before protonation of edge O atoms. Colors indicate O (red), H (pink), Al (light blue), Si (dark blue), and K atoms (purple). In the absence of isomorphic substitutions, the edge surface carries two silanol sites (Oe1, Oe2), one aluminol site (Oe3), and one bridging oxygen (Oe6). The different edge O atoms are labeled on the figure. Isomorphic substitutions of Al for Si near the edge surface give rise to additional types of edge O atoms, listed in parentheses. Brackets indicate regions of the edge surface referred to hereafter as hanging (H) and indented (I). (For interpretation of the references to colour in this figure legend, the reader is referred to the web version of this article.)

The slanted structure of the AC cleavage leads to the formation of two distinct edge sites, which we designate as hanging (H) and indented (I) sites (Fig. 1). Atomic configurations adjacent to these sites differ substantially, leading to the formation of two unique edge-surface coordination environments for adsorbed cations. Our simulations enabled us to distinguish the interactions of these two different sites with aqueous ions (Na, Cs, Cl).

The partial charges of several O atoms on clay edge surfaces (specifically, Oe3, Oe4, Oe5, Oe6, and Oe7) are not defined in the CLAYFF model. Here, we calculated CLAYFF-compatible partial charges for edge oxygen atoms based on an algorithm that accounts for bond valence, charge saturation, and cation charge. In this calculation, we assume that the partial charge on edge oxygen atoms depends on the oxygen valence (−2.00 v.u.) balanced by the total effective charge contributed by coordinating cations *i*:

$$Z^P_{Oej} = -2.00 + \sum_i \frac{N_i(Z_i - Z^P_i)}{CN_i}, \quad (1)$$

where Z_i is the valence of cation *i*, Z_i^P is the partial charge of *i*, N_i is the number of *i* cations coordinating edge oxygen *j*, and CN_i represents the total number of O atoms coordinating cation *i*. This procedure ensures net charge neutrality and captures the expected dependence of the partial charge of edge O atoms on their degree of over- or under-saturation from a bond-valence perspective

Table 2
Partial charges and coordination state of edge O atoms. Other properties of edge O atoms are defined by the CLAYFF model. Octahedral and tetrahedral Al atoms are referred to as Al_O and Al_T, respectively.

Edge site	Site description	Partial charge	B.V.	Cation charge	# Coordinating cations (N_i)			
					Al_O	Si	Al_T	H
Oe1	Hanging ≡Si—OH	−0.95000	2.00	0.95000	–	1	–	1
Oe2	Indented ≡Si—OH	−0.95000	2.00	0.95000	–	1	–	1
Oe3	Octahedral $\equiv Al_O—OH_2$	−0.84760	2.50	1.34760	1	–	–	2
Oe4	Hanging $\equiv Al_T—OH$	−1.06875	1.75	0.81875	–	–	1	1
Oe5	Indented $\equiv Al_T—OH$	−1.06875	1.75	0.81875	–	–	1	1
Oe6	Bridging $\equiv Si—O—Al_O\equiv$	−1.28750	1.50	0.78750	1	1	–	–
Oe7	Bridging $\equiv Al_T—O—Al_O\equiv$	−1.40625	1.25	0.65625	1	–	1	–
Al_O	Octahedral edge Al	1.81250	–	–	–	–	–	–

[99]. A list of edge oxygen sites, their coordination, and calculated partial charges is provided in Table 2.

2.2. Stability of illite edge and basal surfaces

Preliminary MD simulations showed that the doubly-protonated aluminol site $\equiv Al_O—OH_2$ is unstable when simulated as described above. In our preliminary simulations, the $—OH_2$ group frequently detached from the clay surface, perhaps because of its very small net charge of +0.0024 e [+0.425 e for each H atom according to CLAYFF, −0.8476 e for the Oe3 atom according to Eq. (1)]. On the CLAYFF model, O atoms are not strictly bonded to the Al and Si metal centers, so Coulomb interactions are important to the integrity of the clay structure. Supporting quantum mechanical calculations performed using a small muscovite (1 1 0) edge model showed that the detachment of $—OH_2$ groups is not simply an artifact of the MD simulation methodology. These calculations demonstrate that the region mid-way between the $—OH_2$ group and the underlying Al atom has very little electron density (see Supplementary Material). The $\equiv Al_O—OH_2$ bond is distinct from other Al—O(H) bonds, with the charge neutral OH_2 ligand attracted to the aluminum by van der Waals interaction with the permanent OH_2 dipole. These findings are consistent with previous DFT calculations with small pyrophyllite clusters showing that the Al—OH_2 bond is readily broken by thermal motion [59,50]. To account for the weakness of the $\equiv Al_O—OH_2$ bond, we slightly modified the partial charge distribution in the $—OH_2$ group formed by Oe3 atoms to match that of the SPC/E water model. We transferred the small amount of residual charge to the underlying Al atom.

To illustrate the stability of our edge surface model, a snapshot of the 1:1 Na:Cs simulation after 50 ns is shown in Fig. 2. All water molecules are hidden except those that were initially part of the octahedral coordination shell of edge Al atoms. All hydroxyl groups remained bound to the edge surface, while most of the edge water molecules (*i.e.*, $—OH_2$ groups) detached from the surface. A few edge Al atoms (blue) were observed to "pop" out of the structure without becoming completely dissociated. It is apparent that the edges have remained mostly intact throughout the course of the simulation, and there is no evidence of significant instability. Our simulations yield much more stable edge surfaces than other recent MD simulations [66,67], perhaps because the greater negative charge of Oe6 atoms predicted by Eq. (1) helped stabilize $\equiv Si—O—Al_O\equiv$ bridges in our simulations.

Preliminary MD simulations showed that the siloxane surface is unstable if charge-balancing K ions are randomly distributed in the anhydrous interlayers, as noted in Section 2.1. Therefore, we used a newly developed methodology based on stochastic sampling techniques to optimally distribute K ions in the anhydrous interlayers [72]. Our analysis of 20 optimized illite structures suggests that clustering of K ions in regions that contain more Si to Al isomorphic substitutions is energetically favorable. Ionic sites that have at least three neighboring Si atoms substituted by Al are all occupied by K ions.

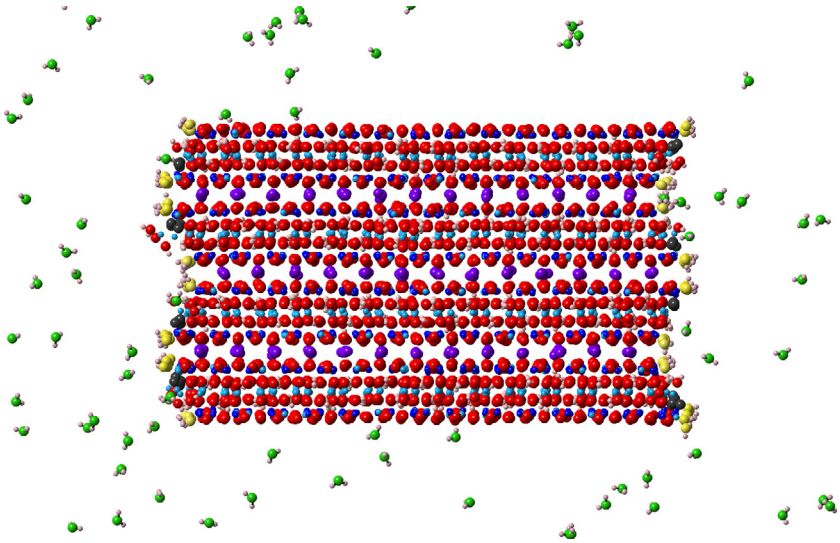

Fig. 2. Molecular dynamics simulation snapshot at the end of a 50 ns production run. Water molecules and Na, Cs, and Cl ions are not shown. Edge oxygen atoms are colored for ease of differentiation: $\equiv Al_O—OH_2$ oxygens (Oe3) are in green; ≡Si—OH and $\equiv Al_T—OH$ oxygens (Oe1, Oe2, Oe4, Oe5) are in yellow; $\equiv Si—O—Al_O\equiv$ and $\equiv Al_T—O—Al_O\equiv$ oxygens (Oe6, Oe7) are in black. Other colors are as in Fig. 1. (For interpretation of the references to colour in this figure legend, the reader is referred to the web version of this article.)

2.3. Molecular dynamics simulations

Standard (unconstrained) MD simulations were carried out to assess the stability of the illite structure and to evaluate the thermodynamics and kinetics of Na—Cs exchange on different surface sites. Briefly, MD simulation trajectories were calculated over intervals in excess of 50 ns for ten different initial aqueous solution compositions at fixed total numbers of electrolyte ions and various mole fraction of Cs^+ ($x_{Cs} = N_{Cs}/(N_{Na} + N_{Cs})$ = 0.1, 0.2, 0.3, 0.4, 0.5, 0.6, 0.7, 0.8, 0.9 and 1.0). The total electrolyte concentration translates to an average ionic strength I = 0.70 ± 0.01 M, equivalent to that of seawater.

All systems were initially equilibrated for 100 ps in the NVE ensemble (fixed number of atoms, volume, and total energy), then for 2 ns in the NPT ensemble (fixed number of atoms, pressure, and temperature). Production runs were performed in the NPT ensemble at P = 0 MPa and T = 298 K. Temperature and pressure were constrained using the Nose-Hoover thermostat and barostat. Newton's equations of motion were solved using the Verlet algorithm with a 1 fs time step. The dynamics of ions and clay atoms were simulated with no constraints (the clay particle was fully flexible). Water molecules were kept rigid using the SHAKE algorithm [80]. Electrostatic and dispersion interactions beyond a cutoff of 15.0 Å were computed by Ewald summation with the particle-particle/particle-mesh (PPPM) method.

2.4. Thermodynamic integration simulations

Based on our MD simulation methodology, thermodynamic integration (TI) calculations were carried out to predict the Gibbs free energies of ion exchange reactions between Na, K, and Cs in bulk liquid water, on illite external basal surfaces, and in anhydrous interlayers. The TI method is routinely used to predict free energies of solvation and the cation binding selectivity of proteins [92,2,32]. Only two MD simulation studies have applied the TI method to predict free energies of cation exchange on clay minerals [97,79]. Both studies focused on the interlayer nanopores of swelling clay minerals. More recently, Okumura et al. [68] used the TI method with DFT simulations of illite frayed edges and predicted that replacement of K by Cs at wedge sites is unfavorable unless the illite basal spacing increases by about 1 Å.

Briefly, our TI calculations consisted in simulating a K-exchanged illite nanoparticle in the NPT ensemble (P = 0 MPa, T = 298 K) using the MD simulation methodology described above. Then, selected K ions on the illite surface were progressively transformed to Na or Cs by modifying their short-range interaction potentials (more precisely, their size and well-depth parameters in the Lennard-Jones 6-12 interaction model) in a series of small steps. Each TI simulation consisted of 15 (K to Cs) or 25 (K to Na) small transformations. Each adjustment to the LJ interaction parameters of the cations of interest was sufficiently small that the total energy of the system changed by less than 2.5 kJ mol^{-1} [92,97]. Each small transformation step was followed by 2.5 ns of equilibration and 1.5 ns of simulation in the NPT ensemble. The absence of hysteresis was verified by carrying out all TI simulations in both directions. Additional calculation details are provided in the Supplementary Material.

In order to examine the cation-exchange selectivity of different surface sites, we carried out four different TI simulations. The first consisted in transforming all cations on the external basal surface of our model illite nanoparticle. The second consisted in transforming all cations in the anhydrous interlayers. The third consisted in transforming a small subset of the interlayer cations in our simulated particle (more precisely, 10 out of 277 interlayer cations). The fourth consisted in transforming a single cation in a simulation cell containing one cation and 999 water molecules.

3. Results and discussion

3.1. Adsorption sites on illite basal and edge surfaces

As described above, we carried out ten MD simulations of NaCl-CsCl mixed electrolytes with a range of Na:Cs ratios to examine the competitive adsorption of Na and Cs on illite edge and basal surfaces. Time integrated Na, Cs, and water O density maps were used to identify ion adsorption sites on illite edge and basal surfaces for each of the 10 simulations. A representative density map for Cs is shown in Fig. 3 for the simulation with a 1:1 Na:Cs ratio. Cesium adsorption occurs preferentially at discrete sites on the basal and edge surfaces. On the basal surfaces, the Cs density maxima are consistent with cesium adsorbing primarily as an inner-sphere surface complex (ISSC) on the ditrigonal cavities of the siloxane sur-

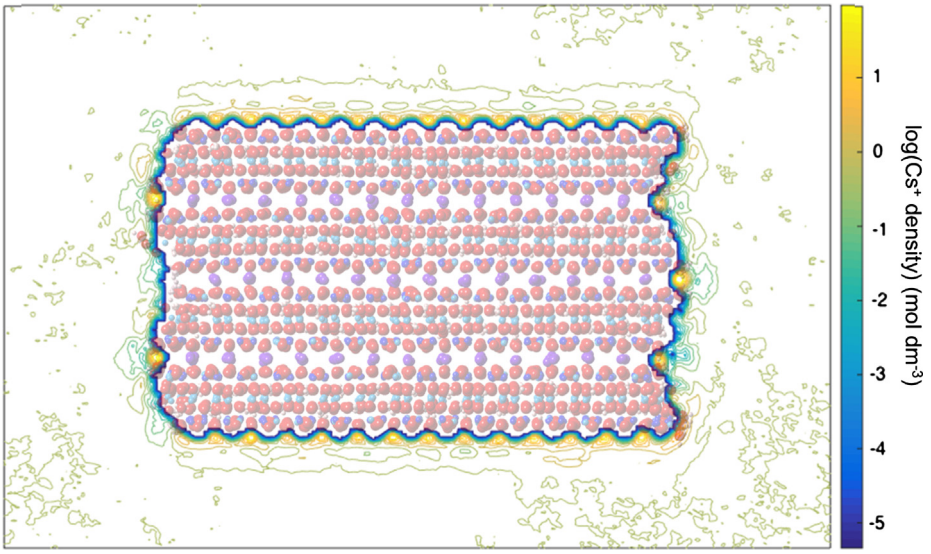

Fig. 3. Map of Cs density averaged over the entire 50 ns simulation with x_{Cs} = 0.5. Cesium primarily binds to ditrigonal cavities on the basal surfaces and to "cleaved cavities" at edge surface H-sites.

face, as shown in previous studies of Cs adsorption on mica [82,52] and smectite [57].

On the edge surface, Cs adsorbs in the plane of the anhydrous interlayers at a distance that matches the periodicity of the distribution of interlayer K ions. Interlayer K ions are located in pockets formed by two ditrigonal cavities on opposite siloxane surfaces. Our results indicate that edge Cs ions adsorb primarily at sites where cleaved pockets are exposed at the edge surface. Our results further show that Cs ions have a much greater affinity for edge H-sites than for edge I-sites, in agreement with the distribution of atomic partial charges in our model of edge O atoms (edge Oe6 and Oe7 atoms, which are closer to the H-site, have more negative charge than edge Oe3 atoms, which are closer to the I-site). Because of the symmetry of the illite structure, positive and negative charge excess sites form neighboring pairs that give the H- and I-sites their distinct adsorption behavior.

One-dimensional atomic density profiles yield further insight into the adsorption mechanisms of Na and Cs on the basal and edge surfaces. Density profiles of Na and Cs on the basal surfaces are given in Fig. 4a and b for low (x_{Cs} = 0.1) and high (x_{Cs} = 0.9) Cs end-member simulations. Density profiles adjacent to the basal surfaces are broadly consistent with the triple layer model (TLM) of the electrical double layer (EDL), whereby adsorbed ions form inner- or outer-sphere surface complexes (ISSC, OSSC) or take part in the diffuse ion swarm, *i.e.*, adsorbed ions form distinct species separated from the surface by zero, one, or more than one layers of water molecules [38,39,12]. Cesium adsorbs almost exclusively as a single type of ISSC, as observed experimentally on the basal surface of mica [52]. Sodium has a more complex behavior: based on the relative location of Na and water density peaks in Fig. 4, Na forms two types of ISSC as well as an OSSC. Our finding that Na forms primarily ISSC on illite supports the emerging view that electrolyte ions can adsorb significantly as ISSC, in contradiction with the prevailing assumption in surface complexation models based on the triple layer model that restricts these species to OSSC and the diffuse swarm. The Cl density profile shows a significant density peak in Fig. 4a, suggesting that CsCl ion pairs have a significant affinity for illite basal surfaces.

To a first approximation, the location of ISSC should be determined primarily by the size of the adsorbed ion [75,77,51]. For consistency with previous studies, we define the location of adsorbed ions on the illite basal surface as the distance $z*$ from the position of the plane of surface O atoms. The density peak of Na ISSC (z^* = 1.25 Å) is much closer to that surface than expected based on the sum of the hard-sphere radii of O and Na atoms ($r_O \approx 1.6$ and $r_{Na} \approx 1.3$ Å according to the interatomic potential parameters used in the present study). This large difference indicates that Na ions are deeply ensconced in the ditrigonal cavities of the siloxane surface. The Cs density peak is located further from the plane of basal surface O atoms (z^* = 2.26 Å) in agreement with its larger hard-sphere radius ($r_{Cs} \approx 1.9$ Å). A smaller fraction of the hard-sphere radius of Cs sits below the basal surface indicating that Cs ions do not fit as snugly in the ditrigonal cavities as does Na.

The location of the Cs density peak in Fig. 4 is remarkably consistent with the peak position measured by X-ray reflectivity for Cs ions adsorbed at the mica-water interface, z^* = 2.26 ± 0.01 Å [52]. In the case of Na, experimental measurements of the location of adsorbed ISSC do not exist. However, the two ISSC peaks are located much closer to the surface than in previous MD simulations carried out with a rigid clay structure. For example, Bourg and Sposito [12] observed Na ISSC at z^* = 2.6 Å in MD simulations of Na-smectite carried out with the same set of interatomic potential parameters. The difference is likely due to the isomorphic substitutions being located in the tetrahedral sheet (closer to the basal surface than in studies of smectite clay minerals) and, also, to the simulations presented here being performed using a flexible clay structure. The CLAYFF model, when used to model flexible phyllosilicate sheets, is known to predict an unphysical relaxation of the siloxane surface that transforms the ditrigonal cavities to larger hexagonal cavities [107]. The deep entry of Na in the hexagonal cavities is an artifact of this unphysical relaxation.

On the edge surfaces, we calculated atomic density profiles as a function of distance from the surface in two equally sized regions centered on the H and I edge sites. Because of the corrugated topography of the edge surface, the choice of reference plane where z = 0 is somewhat arbitrary. In Fig. 5, this plane was chosen as the location of closest approach of water O atoms. With this choice of reference plane, ions located at z values smaller than about 3 Å form ISSC, while ions located at z values of about 3–6 Å form OSSC. Ion density profiles shown in Fig. 5 confirm that Cs ions adsorb primarily as ISSC on both H- and I-sites. Sodium ions adsorb only on the H-sites and they have a small preference for forming OSSC rather than ISSC. In each cation density profile, the low density between ISSC and OSSC suggests the presence of an energy barrier to edge ion exchange.

3.2. Cs adsorption selectivity on basal and edge surfaces predicted by MD simulation

Cation adsorption on different illite surface sites was quantified as a surface excess (n_i^w, mol m^{-2}) using the well established formulation [89]:

$$n_i^w = \frac{1}{A}\left[N_i - c_i V^{fl}\right], \tag{2}$$

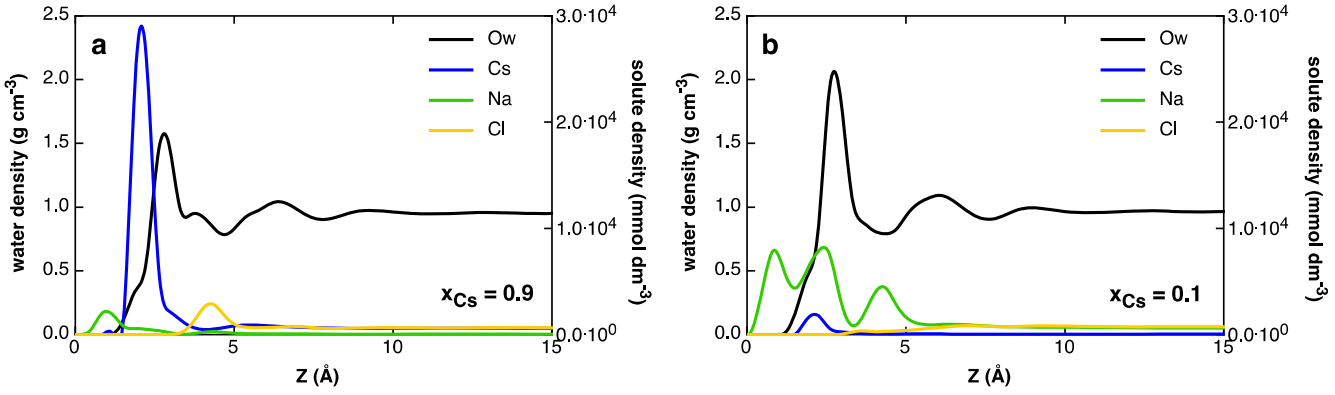

Fig. 4. Density profiles of solutes (Na, Cs, and Cl) and water oxygen atoms (Ow) adjacent to illite basal surfaces during our 50 ns simulations at x_{Cs} = 0.9 (a) and x_{Cs} = 0.1 (b). Distances (z) are reported relative to the distance where all solute and solvent ion concentrations go to zero.

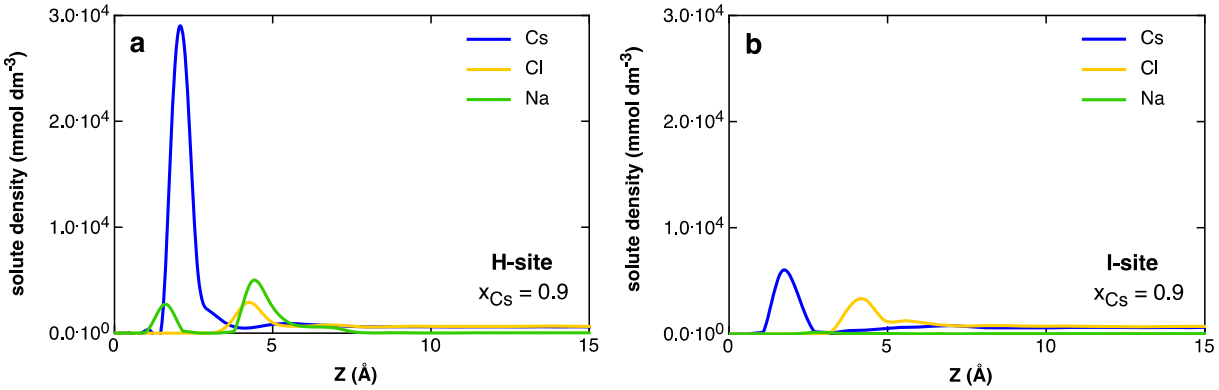

Fig. 5. Density profiles of adsorbed ions adjacent to hanging (a) and indented (b) sites on the illite edge surface.

where A (m^2), N_i (moles), c_i (mol m^{-3}) are the interfacial area of a given site-type, moles of i in volume V^{fl} (m^3) adjacent to the site, and bulk aqueous concentration of i far from the surface. Eq. (2) allows a direct comparison of the average density of adsorbed cations on each site (irrespective of adsorption mechanism) in units of moles per m^2. Macroscopic measurements of adsorption are often reported as a specific surface excess over the entire solid phase, referred to here as $(n_i^w)_{macro}$ in mol kg^{-1} [89]. If the specific surface area contributed by different types of surfaces ($a_{s,basal}$, $a_{s,H\text{-}edge}$, and $a_{s,I\text{-}edge}$ in m^2/kg) is known, the value of $(n_i^w)_{macro}$ can be predicted from the molecular-scale values of n_i^w on each type of surface (in mol m^{-2}):

$$(n_i^w)_{macro} = (a_s n_i^w)_{basal} + (a_s n_i^w)_{H-edge} + (a_s n_i^w)_{I-edge}. \quad (3)$$

In the simulations performed here, $a_{s,basal} = 1.76 \times 10^5$ m^2/kg and $a_{s,H\text{-}edge} = a_{s,I\text{-}edge} = 5.56 \times 10^4$ m^2/kg, where edge *H*- and *I*-site surfaces are defined such that their respective areas are equal to half of the total edge area. Surface, edge-site specific, and total particle values for Na and Cs surface excess are summarized in Table EA2 (Supplementary Material) for each of the 10 MD simulations performed. The data are plotted as adsorption isotherms for basal and edge surfaces in Fig. 6.

3.2.1. Geochemical modeling

We used a single geochemical model to describe the adsorption results shown in Table EA2, Figs. 6, and 7. In this model, Cs adsorption on a cation exchange site of Na-illite is described with the equation

$$XNa^+(S) + Cs^+(aq) \leftrightarrow XCs^+(s) + Na^+(aq), \quad (4)$$

with the corresponding mass action equation [11],

$$K_{eq}^{Na/Cs} = \frac{a_{Na} a_{XCs}}{a_{Cs} a_{XNa}}. \quad (5)$$

Here, we assume that the activity coefficients of surface sites are proportional to their mole fraction on the surface (x) times an activity coefficient (γ). This yields:

$$a_{Xi} = \gamma_{Xi} x_i \quad (6)$$

We use the regular solution model to describe surface solution behavior,

$$\gamma_{Xi} = \exp\left(\alpha x_{Xj}^2\right) \quad (7)$$

where for a mixture of adsorbed ions i and j, x_{Xi} is the fraction of X sites occupied by adsorbed ion i ($x_{Xi} = n_i/(n_i + n_j)$), and α is a free parameter that captures the excess free energy of mixing of surface Na and Cs. This model can be used to describe the thermodynamics of binary solid solutions [48] and assumes that the excess free energy of mixing is entirely due to enthalpic effects. If $\alpha = 0$, the regular solution model simplifies to the ideal surface solution model. Eqs. (4)–(6), when combined with a mass balance on surface sites (*i.e.*, $n_{tot} = n_i + n_j$), yield the following expressions for the specific surface excesses of Na and Cs:

$$n_{Na} = \frac{n_{tot}}{1 + K_{eq}^{Na/Cs} \frac{a_{Cs}\gamma_{XNa}}{a_{Na}\gamma_{XCs}}} \quad (8)$$

$$n_{Cs} = \frac{n_{tot}}{1 + \frac{1}{K_{eq}^{Na/Cs}} \frac{a_{Na}\gamma_{XCs}}{a_{Cs}\gamma_{XNa}}}. \quad (9)$$

If the activity coefficients of adsorbed species are unknown, Eq. (5) can be replaced with an empirical model such as the Vanselow selectivity model [101]:

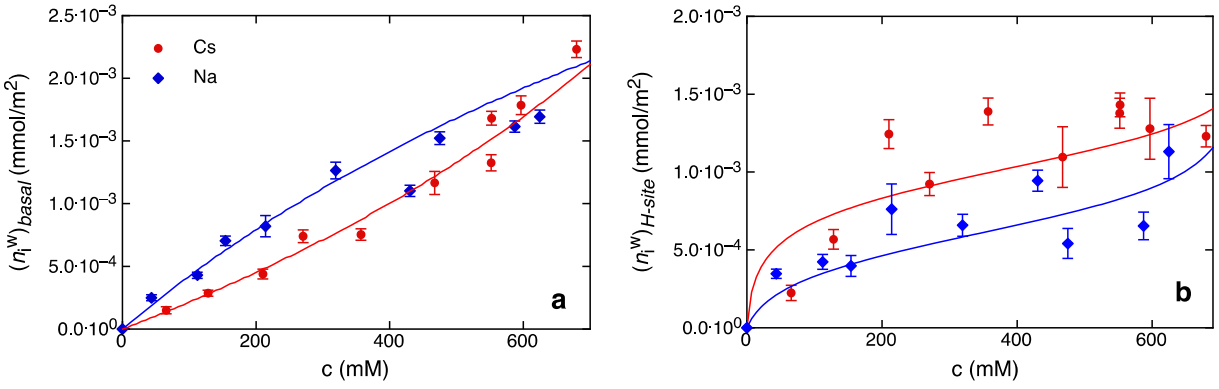

Fig. 6. Adsorption isotherms for Na (blue diamonds) and Cs (red circles) determined from the ten 50 ns MD simulation runs on (a) basal surfaces and (b) edge H-sites. Isotherms were fitted using the thermodynamic model Eqs. (8) and (9). (For interpretation of the references to colour in this figure legend, the reader is referred to the web version of this article.)

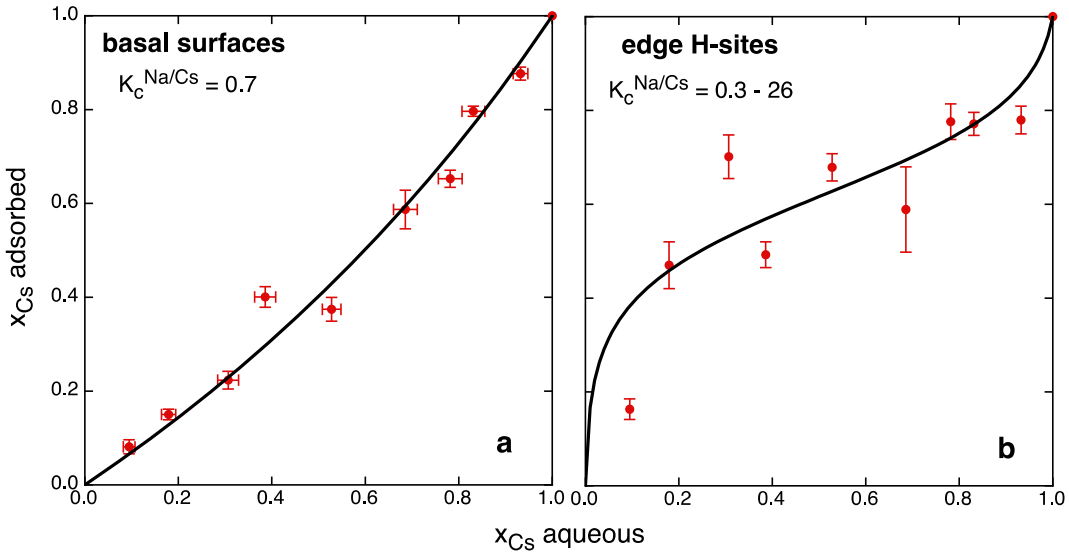

Fig. 7. Na—Cs exchange isotherms for (a) basal and (b) edge sites. Basal exchange behavior is consistent with an ideal surface solution, while edges exhibit non-ideal exchange behavior. Edges are significantly Cs-selective at low Cs surface loadings but become increasingly Na-selective as the aqueous mole fraction of Cs approaches 1.0.

$$K_V^{Na/Cs} = \frac{a_{Na}x_{XCs}}{a_{Cs}x_{XNa}}. \quad (10)$$

where the Vanselow selectivity coefficient, K_V, may vary with experimental conditions unless surface solution behavior is ideal. For ideal surface solutions, the ratio of surface activities is equivalent to the ratio of surface excess concentrations and K_V becomes equal to the thermodynamic equilibrium constant K_{eq}. Finally, if the activity coefficients of dissolved species are unknown, a conditional selectivity coefficient (K_c) can be defined that is expressed in terms of measurable quantities including aqueous and surface species concentrations,

$$K_c^{Na/Cs} = \frac{c_{Na}x_{XCs}}{c_{Cs}x_{XNa}}. \quad (11)$$

This equation follows immediately from Eq. (10) if the Davies equation is used to model activity coefficients of aqueous species. For ideal surface solutions, Eqs. (5), (10) and (11) yield the relation: $K_{eq}^{Na/Cs} = K_V^{Na/Cs} = K_c^{Na/Cs}(\gamma_{Na}/\gamma_{Cs})$.

3.2.2. Sorption on basal and edge surface sites

Adsorption isotherms calculated with Eqs. (8) and (9) are plotted in Fig. 6 for basal and edge surfaces. For simplicity, we assumed that aqueous Na and Cs have identical activity coefficients. Model curves were fitted using unconstrained nonlinear optimization of two parameters: $K_{eq}^{Na/Cs}$, and α. The total site capacities of basal and edge H-site surfaces (n_{tot} = 2.17 ± 0.02 μmol m^{-2} and 1.66 ± 0.18 μmol m^{-2} 2 s.e., respectively) were determined based on the average combined surface occupancy by Na and Cs in all MD simulations.

In the case of illite basal surfaces (Fig. 6a), adsorption of Na and Cs is approximately linear in the simulated concentration range, in other words, adsorption is consistent with a linear partitioning coefficient $K_d = n_i/C_i$, where C_i is the aqueous concentration of ion *i*. The optimized surface solution activity parameter α was very close to 0 (α = 0.01 and −1.2 < α < 0.3, 2 s.e.), indicating that ion exchange on the basal surfaces follows ideal solution behavior. This near-ideality indicates that Na—Cs exchange on illite basal surfaces is not significantly influenced by lateral interactions between adsorbed cations, in agreement with a previous MD simulation study of Na—Cs exchange in smectite interlayers [79]. The best fit was obtained with $K_{eq}^{Na/Cs}$ = 0.7 (0.6 < $K_{eq}^{Na/Cs}$ < 0.8, 2 s.e.), indicating that the basal surface is essentially non-selective or slightly selective towards Na. This behavior contrasts with the experimentally observed selectivity of illite basal surfaces towards Cs over Na (Table 1). A plausible explanation is that the unphysical relaxation of ditrigonal cavities on the basal surface in our model illite nanoparticle (noted in Section 3.1) results in our model overestimating the affinity of Na for the illite basal surface.

Ion adsorption on edge H-sites is distinctly different from that observed on the basal surfaces (Fig. 6b). Calculated errors on surface excess values are larger than those associated with the basal adsorption isotherms, because the smaller number of exchange sites and slower exchange kinetics on the edge surfaces (described below) result in poorer statistics. For edge H-sites, the optimized α = −2.2 is significantly different from zero (−5.8 < α < −0.8, 2 s.e.) indicating that edges are characterized by non-ideal surface solution behavior. The optimized exchange equilibrium constant, $K_{eq}^{Na/Cs}$ = 2.8 (1.6 < $K_{eq}^{Na/Cs}$ < 5.0, 2 s.e.), is larger than its basal sorption counterpart. The non-ideal adsorption behavior characteristic of the edge sites indicates that their selectivity behavior depends upon the aqueous solution composition (in particular, on the mole fraction of Cs in the aqueous phase).

3.2.3. Ion exchange on basal and edge surface sites

Exchange selectivity behavior can be illustrated by plotting the aqueous vs. solid mole fractions of Cs (Fig. 7). In this framework, an ideal non-selective isotherm will follow the 1:1 line, a Na-selective isotherm falls below the 1:1 line, and a Cs-selective isotherm falls above the 1:1 line. The conditional selectivity of basal surfaces is modeled in Fig. 7a based on Eq. (11) with a $K_c^{Na/Cs} = 0.73 = K_{eq}^{Na/Cs}$. The results indicate that the simulated illite basal surface is slightly Na-selective. The value of $K_c^{Na/Cs}$ on basal surfaces is invariant with x_{Cs} and equal to the calculated equilibrium constant for Eq. (5), in agreement with the ideal surface solution model. The exchange isotherm for the edge H-sites is plotted in Fig. 7b along with the conditional selectivity model (Eq. (11)), where adsorption to the edges for Na and Cs is described by their respective adsorption isotherms (Eqs. (8) and (9). The adsorption selectivity of I-sites was not calculated, because values of Cs and Na surface excess at these sites were typically within error of zero. In stark contrast to the adsorption behavior observed on basal surfaces, Na—Cs exchange at edge H-sites is non-ideal, resulting in a $K_c^{Na/Cs}$ value that varies with x_{Cs}. Based on the fitted selectivity model, edge

H-sites are Cs-selective ($K_c^{Na/Cs} = 26$) in low-Cs solutions ($c_{Cs} < 1$ mM) and Na-selective ($K_c^{Na/Cs} = 0.31$) in high-Cs solutions ($c_{Cs} = 0.7$ M).

Cation exchange reactions involving Cs adsorption on illite and smectite are known to be non-ideal, but this non-ideality has been attributed in the past to variations in water activity with changes in salinity and interlayer spacing [54,79,11]. In our simulations, insight into the non-ideality of edge ion exchange can be gained by scrutinizing Cs adsorption behavior at H-sites. Ions located in the density maximum location in Fig. 5a are bound to the H-sites as ISSC. With increasing aqueous mole fraction of Cs, the capacity of these sites for monovalent cations (Na + Cs) actually increases from approximately 0.5 ions per site at $x_{Cs} = 0.1$ to approximately 0.7 ions per site at $x_{Cs} = 1.0$. The significant increase in H-site occupancy by inner-sphere complexed ions suggests that Cs changes the structure of the site itself, causing the observed non-ideal adsorption behavior.

3.3. Cs adsorption selectivity in anhydrous interlayers predicted by TI simulation

As noted above, Cs entry in anhydrous illite interlayers was not observed during our ten 50 ns MD simulation, in agreement with the very slow kinetics of Cs adsorption on the illite slow site [21,22]. To complement our unconstrained MD simulation results, we used the thermodynamic integration (TI) technique to predict the Gibbs free energy change associated with alchemical transformations of Na to Cs in bulk liquid water, on external basal surfaces, and in anhydrous interlayers. More precisely, our calculations yielded the free energy change $\Delta G^{Na/i}$ associated with the replacement of Na by *i*, where *i* = K or Cs. The difference between our predicted values of $\Delta G^{Na/i}$ on the surface ($\Delta G_{ads}^{Na/i}$) and in solution ($\Delta G_{aq}^{Na/i}$) yields the Gibbs free energy of the cation exchange reaction between Na and *i* ($\Delta G_{ex}^{Na/i}$):

$$\Delta G_{ex}^{Na/i} = \Delta G_{ads}^{Na/i} - \Delta G_{aq}^{Na/i}. \quad (15)$$

From our predicted values of $\Delta G_{ex}^{Na/i}$, we calculated the ion-exchange selectivity coefficient between Na and *i* with the relation:

$$K_{eq}^{Na/i} = \exp\left(-\Delta G_{ex}^{Na/i}/RT\right), \quad (16)$$

where *R* is the ideal gas constant and *T* = 298 K. Our predicted values of $\Delta G_{aq}^{Na/K} = 73 \pm 1$ kJ mol^{-1}, $\Delta G_{aq}^{Na/K} = 89 \pm 1$ kJ mol^{-1}, and $\Delta G_{aq}^{Na/Cs} = 113 \pm 1$ kJ mol^{-1} are almost equal to the experimental values of 70, 90, and 115 kJ mol^{-1}, respectively [56]. Our predicted values of the free energy of exchange are reported in Fig. 8 as a function of $\Delta G_{aq}^{Na/i}$ (the free energy of hydration relative to the value for sodium). The values for Na, K, and Cs are highlighted with larger symbols. Values of log K_{eq} calculated from the results presented in Fig. 8 are shown in Table 3.

Our TI simulations predict that Na—Cs exchange on illite basal surfaces is essentially non-selective. This result is consistent with the ion exchange isotherm shown in Fig. 7a and confirms that our 50 ns MD simulations with mixed NaCl-CsCl electrolytes were sufficiently long to probe equilibrium adsorption on the basal surfaces. As noted above, the non-selective nature of Na—Cs exchange on illite basal surfaces is likely an artifact related to the unphysical relaxation of the siloxane surface cavities predicted by the CLAYFF model. The use of a rigid mineral structure in simulations of ion adsorption on the basal surface of mica (unpublished) resulted in a decreased tendency of Na^+ ions to drop deeply within the hexagonal cavities, a better agreement with X-ray reflectivity data, and less affinity of Na for the basal surfaces ($\log K_{eq}^{Na/Cs} \sim 2$).

The results shown in Table 3 indicate that the anhydrous interlayer nanopores have a high selectivity for weakly hydrated cations (K, Cs). The predicted value of log $K_{ex}^{Na/Cs}$ in anhydrous interlayers is lower than obtained by DFT simulations of mica at 300 K [log $K_{eq}^{Na/Cs} \approx 4.0$ [93]] and lower than the values reported for the high affinity sites (Table 1). The difference is consistent with the unphysical relaxation of surface ditrigonal cavities in our MD simulations

Table 3
Cation exchange selectivities of the basal surfaces and anhydrous interlayers predicted by our TI calculations. The third column corresponds to the replacement of all interlayer K ions; the fourth column corresponds to the replacement of a small number of K ions (< 3%) dispersed in the three interlayers. Confidence intervals are reported as ±2σ.

Site type	Basal	Interlayer	Interlayer (trace)
log $K_{eq}^{Na/Cs}$	−0.1 ± 0.1	2.2 ± 0.1	1.1 ± 0.1
log $K_{eq}^{K/Cs}$	−0.4 ± 0.1	−0.7 ± 0.1	−2.9 ± 0.1

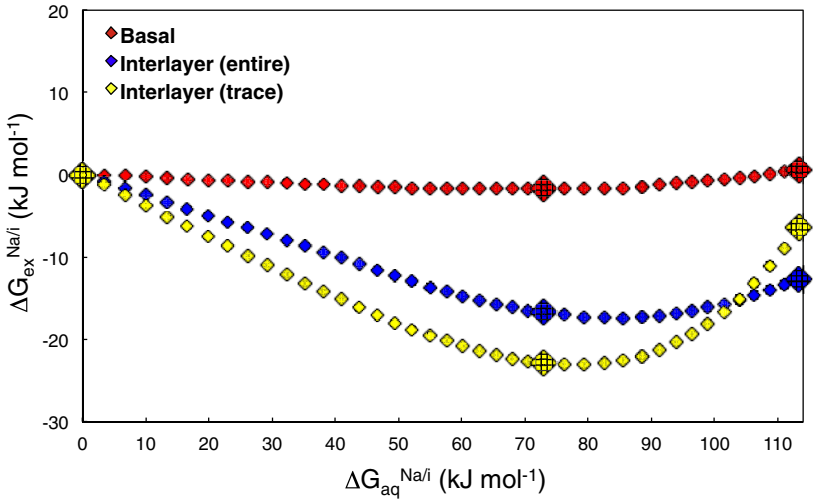

Fig. 8. Thermodynamic integration (TI) prediction of the Gibbs free energy of cation exchange (relative to Na) as a function of the Gibbs free energy of hydration (relative to Na). The different colors show results obtained at three different sites on the illite surface: on the external basal surface (red), in collapsed interlayers where all interlayer ions are simultaneously transformed (blue), and in collapsed interlayers where most ions remain K^+ while a few dispersed ions are transformed (yellow). Large symbols show free energies obtained for Na, K, and Cs (from left to right); smaller symbols show the intermediate steps of the alchemical transformations. Error bars are smaller than the symbols. (For interpretation of the references to colour in this figure legend, the reader is referred to the web version of this article.)

causing a significant overestimation of the affinity of Na for the external basal surfaces. Our simulations predict that adsorption in the interlayers has very little selectivity between K and Cs, in agreement with DFT calculations [68,93]. For example, DFT simulations of mica at 300 K yielded Helmholz free energies of exchange consistent with log $K_{eq}^{K/Cs} \approx -0.6$ [93] a value essentially equal to our prediction. Our results demonstrate for the first time that the specific affinity of interlayer sites for K ions relative to other alkaline metals of smaller and larger size is in essence a "Goldilocks" effect, indicating that the K^+ ion has an optimal size to accommodate these sites. This effect explains why K concentration in soils is a good predictor of the abundance of illitic clay minerals.

Finally, our TI calculations provide evidence of a strong driving force for cation segregation in collapsed illite interlayers: K—Cs exchange has little selectivity if the entire population of interlayer cations is transformed from K to Cs, but it is highly unfavorable (by 16.4 ± 0.7 kJ mol^{-1}) if only a few K ions are exchanged for Cs in an otherwise K-filled interlayer. This strong selectivity difference likely derives from the fact that, during replacement of the interlayer population of interlayer cations, the collapsed interlayer adjusts its basal spacing to accommodate the size of the interlayer cations. If only a few K ions are replaced by Cs in an otherwise K-filled interlayer, the large population of interlayer K ions imposes a basal spacing that is too small to comfortably accommodate Cs.

3.4. Ion exchange kinetics on basal and edge surfaces

Molecular dynamics simulation results were used to investigate the kinetics of ion exchange at basal and edge surface sites using a waiting time distribution technique analogous to a 1D jump diffusion model [12,57]. Over the course of these simulations, no ions migrated from the bulk solution to the interlayer or within the interlayer itself due to significant energetic barriers to interlayer ion exchange. The dynamics of interlayer ion exchange will be the subject of future work. We determined the amount of time that Na and Cs ISSC reside in the vicinity of each individual site type (basal, H-, and I-) to compare element- and site-specific exchange dynamics. Positions of high affinity Na and Cs sorption sites were identified using density maps integrated over the entire simulation time. Geometries of inner-sphere edge sites differed from those of basal sites, so exchange events at these sites were calculated in a slightly different way. Ions were assumed to have left (or entered) an edge site when crossing out of (or into) a cylindrical zone with 2 Å radius surrounding the Cs or Na site, a sufficiently large size to encompass edge ISSC. Ion exchange events involving a hop along the edge were not counted. Basal surface ion exchange events were counted when an ion left or entered a slab within 3 Å of the closest-approaching Na^+ ions, which approximately separates inner- and outer-sphere surface complexes for both Cs and Na (Fig. 4a). For each type of site, we calculated the distribution of ion residence times between exchange events (Fig. 9), as well as the time within which 90% of the Na or Cs ions leave the site (Table 4). We refer to the latter quantity as τ_{90}. This approach enables us to directly compare the ion exchange fluxes between sites for both Na and Cs.

The typical distribution of ion residence times included a high probability of exchange over short timescales (*i.e.*, many transient visits to the site) and a low probability of exchange over long timescales, on order of the duration of the entire simulations (*i.e.*, few prolonged visits to the site). An example histogram of residence times is plotted for Na and Cs on basal surfaces and edge H- and I-sites for the x_{Cs} = 0.5 simulation in Fig. 9. The τ_{90} values for each ion and site type averaged over all ten simulations are listed in Table 4. On average, Na and Cs τ_{90} residence times on the basal surfaces are within error of one another at 0.30 ± 0.03 ns and 0.34 ± 0.03 ns, respectively. In contrast, the average τ_{90} value of Cs ions at edge H-sites (7.25 ± 2.34 ns) is considerably longer than that of Na ions at the same sites (0.82 ± 0.47 ns). The same may be true for edge I-sites (2.93 ± 2.83 ns for Cs and 0.22 ± 0.07 ns for Na) except that the large errors for Cs make the values nominally equal. The results shown in Table 4 indicate that Cs binding at edge sites, in addition to being thermodynamically favored, is considerably more stable than for Na. The results also confirm the necessity of simulating several tens of nanoseconds to reach complete

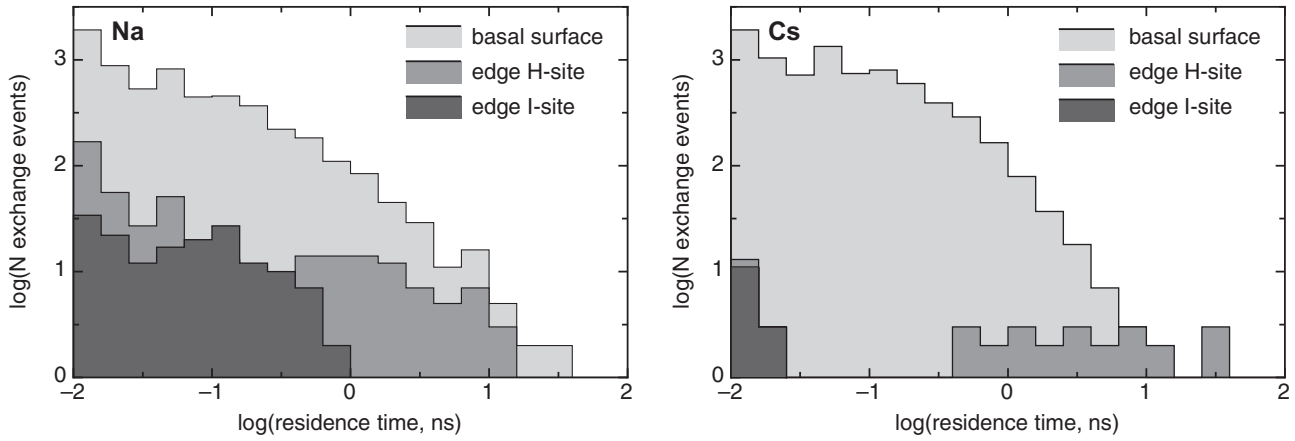

Fig. 9. Histogram of Na^+ (left) and Cs^+ (right) residence times at edge and basal sites. Exchange dynamics of Cs^+ at edge H-sites are highly skewed towards long (nm) residence times compared with the fast-exchanging Na^+.

Table 4
Average timescales over which 90% of inner-sphere complexed ions exchanged with outer-sphere or diffuse swarm ions. Reported values are averaged over all ten simulations with different Na/Cs ratios. Confidence intervals are reported as ±2σ.

Na			Cs		
τ_{90} basal (ns)	τ_{90} edge H-site (ns)	τ_{90} edge I-site (ns)	τ_{90} basal (ns)	τ_{90} edge H-site (ns)	τ_{90} edge I-site (ns)
0.30 ± 0.03	0.82 ± 0.47	0.22 ± 0.07	0.34 ± 0.03	7.25 ± 2.34	2.93 ± 2.83

exchange equilibrium with respect to Cs at edge H-sites. The much poorer statistics for edge compared to basal sites arises from the fact that there are many more available basal sorption sites in each simulation.

4. Conclusions

Molecular dynamics simulations of a new fully-flexible illite structure displaying edge, basal, and interlayer sites give Na/Cs sorption selectivities broadly consistent with the range of existing experimental data. Cesium sorbed to the exterior surfaces of illite form primarily ISSC at both basal and edge sites, while both Na and Cs form ISSC on basal surface sites adjacent to ditrigonal cavities on the siloxane surface, similar to existing X-ray reflectivity data. Ion exchange proceeds relatively rapidly for both Na and Cs at basal sites, in stark contrast with the slow exchange dynamics of Cs at edge sites, indicating a source of the high affinity for Cs at edges. Interlayer ions were found to be non-exchangeable over the timescale of the MD simulations reported here (50 ns), so thermodynamic integration calculations were performed instead to investigate the affinity of Cs for interlayer sites. These TI calculations demonstrate that complete K/Cs exchange in the interlayer sites is weakly selective and that there is a strong thermodynamic preference for Cs relative to Na in anhydrous interlayers. Exchange of trace interlayer K for Cs is highly unfavorable compared with complete replacement of K for Cs, revealing a strong driving force for interlayer ion stratification upon migration of Cs to slow sites. Together, these findings suggest that previously identified slow sites are likely located in the interlayers of micaceous clays, as hypothesized. The kinetics of interlayer ion exchange are not possible to resolve in these 50 ns MD simulations and will be the subject of a future study.

Geochemical modeling of the simulated adsorption and selectivity data reveals a fundamentally different ion adsorption behavior at edge and basal adsorption sites that had not previously been resolved, because of the difficulty of isolating these sites experimentally. In particular, adsorption at edge sites is shown to be non-ideal due to the impact of high Cs concentrations on edge site capacities, and edge sites are Cs selective at low Cs loadings. We conclude that the flexible model presented here is a substantive advance on existing models as it enables simultaneous investigation of molecular-level mechanisms governing ion exchange on various sites, including edge sites. Future studies will make use of this structure, which also allows for edge expansion, to specifically address the mechanisms of high-affinity frayed edge site formation. Alternative simulation techniques including metadynamics will be useful to elucidate the thermodynamics and mechanisms of frayed edge site formation.

Acknowledgements

The authors gratefully acknowledge support for this research from the Japan Atomic Energy Agency (JAEA)-LBNL Collaboration on Repository Geoscience and PA Technology Development. IB was partly supported by the Office of Science, Office of Basic Energy Sciences of the US Department of Energy under Contract DE-AC02-05CH11231. The MD and TI simulations reported in this paper were carried out using resources of the National Energy Research Scientific Computing Center (NERSC), which is supported by the Office of Science of the US Department of Energy under Contract DE-AC02-05CH11231. The DFT simulations were carried out using the SGI ICE X supercomputer at the Japan Atomic Energy Agency. GS was supported by funds allocated through his appointment as Chancellor's Professor, Emeritus, University of California, Berkeley.

Appendix A. Supplementary material

Supplementary data associated with this article can be found, in the online version, at http://dx.doi.org/10.1016/j.jcis.2016.11.084.

References

[1] S.J. Anderson, G. Sposito, Cesium-adsorption method for measuring accessible structural surface charge, Soil Sci. Soc. Am. J. 55 (1991) 1569–1576.
[2] J. Åqvist, Ion-water interaction potentials derived from free energy perturbation simulations, J. Phys. Chem. 94 (1990) 8021–8024.
[3] B. Baeyens, M.H. Bradbury, Cation exchange capacity measurements on illite using the sodium and cesium isotope dilution technique: effects of the index cation, electrolyte concentration and competition: modeling, Clays Clay Miner. 52 (2004) 421–431.
[4] A. Benedicto, T. Missana, A.M. Fernández, Interlayer collapse affects on cesium adsorption onto illite, Environ. Sci. Technol. 48 (2014) 4909–4915.
[5] H.J.C. Berendsen, J.R. Grigera, T.P. Straatsma, The missing term in effective pair potentials, J. Phys. Chem. 91 (1987) 6269–6271.
[6] L. Bergaoui, J.F. Lambert, R. Prost, Cesium adsorption on soil clay: macroscopic and spectroscopic measurements, Appl. Clay Sci. 29 (2005) 23–29.
[7] B.R. Bickmore, K.M. Rosso, K.L. Nagy, R.T. Cygan, C.J. Tadanier, Ab initio determination of edge surface structures for dioctahedral 2:1 phyllosilicates: implications for acid-base reactivity, Clays Clay Miner. 51 (2003) 359–371.
[8] B.C. Bostick, M.A. Vairavamurthy, K.G. Karthikeyan, J. Chorover, Cesium adsorption on clay minerals: an EXAFS spectroscopic investigation, Environ. Sci. Technol. 36 (2002) 2670–2676.
[9] I.C. Bourg, G. Sposito, A.C.M. Bourg, Modeling the acid-base surface chemistry of montmorillonite, J. Colloid Interface Sci. 312 (2007) 297–310.
[10] I.C. Bourg, G. Sposito, Connecting the molecular scale to the continuum scale for diffusion processes in smectite-rich porous media, Environ. Sci. Technol. 44 (2010) 2085–2091.
[11] I.C. Bourg, G. Sposito, Ion exchange phenomena, in: Handbook of Soil Science, Properties and Processes, 2nd ed., P.M. Huang, Y. Li, M. E. Sumner (eds.), CRC Press, Chapter 16, 2011a.
[12] I.C. Bourg, G. Sposito, Molecular dynamics simulations of the electrical double layer on smectite surfaces contacting concentrated mixed electrolyte (NaCl-$CaCl_2$) solutions, J. Colloid Interface Sci. 360 (2011) 701–715.
[13] I.C. Bourg, C.I. Steefel, Molecular dynamics simulations of water structure and diffusion in silica nanopores, J. Phys. Chem. C 116 (2012) 1156–11564.
[14] M.H. Bradbury, B. Baeyens, A generalised sorption model for the concentration dependent uptake of caesium by argillaceous rocks, J. Contam. Hydrol. 42 (2000) 141–163.
[15] E. Brouwer, B. Baeyens, A. Maes, A. Cremers, Cesium and rubidium ion equilibria in illite clay, J. Phys. Chem. 87 (1983) 1213–1219.
[16] S.A. Carroll, J.V. Walther, Kaolinite dissolution at 25°, 60°, and 80 °C, Am. J. Sci. 290 (1990) 797–810.
[17] Z. Chen, G. Montavon, S. Ribet, Z. Guo, J.C. Robinet, K. David, C. Tournassat, B. Grambow, C. Landesman, Key factors to understand in-situ behavior of Cs in Callovo-Oxfordian clay-rock (France), Chem. Geol. 387 (2014) 47–58.
[18] J. Chorover, M. DiChiaro, O. Chadwick, Structural charge and cesium retention in a chronosequence of tephritic soils, Soil Sci. Soc. Am. J. 63 (1999) 169–177.
[19] S.V. Churakov, Ab initio study of sorption on pyrophyllite: structure and acidity of the edge sites, J. Phys. Chem. B 110 (2006) 4135–4146.
[20] R.N.J. Comans, J.J. Middelburg, J. Zonderhuis, J.R.W. Woittiez, G.J. De Lange, H. A. Das, C.H. Van Der Weijden, Mobilization of radiocaesium in pore water of lake sediments, Nature 339 (1989) 367–369.
[21] R.N.J. Comans, M. Haller, P. De Preter, Sorption of cesium on illite: non-equilibrium behaviour and reversibility, Geochim. Cosmochim. Acta 55 (1991) 433–440.
[22] R.N.J. Comans, D.E. Hockley, Kinetics of cesium sorption on illite, Geochim. Cosmochim. Acta 56 (1992) 1157–1164.
[23] R.T. Cygan, J.-J. Liang, A.G. Kalinichev, Molecular models of hydroxide, oxyhydroxide, and clay phases and the development of a general force field, J. Phys. Chem. B 108 (2004) 1255–1266.
[24] L.X. Dang, Mechanism and thermodynamics of ion selectivity in aqueous solutions of 18-crown-6 ether: a molecular dynamics study, J. Am. Chem. Soc. 177 (1995) 6954–6960.
[25] A. de Koning, R.N.J. Comans, Reversibility of radiocaesium sorption on illite, Geochim. Cosmochim. Acta 68 (2004) 2815–2823.
[26] L. Dzene, E. Tertre, F. Hubert, E. Ferrage, Nature of the sites involved in the process of cesium desorption from vermiculite, J. Colloid Interface Sci. 455 (2015) 254–260.
[27] D.D. Eberl, Alkali cation selectivity and fixation by clay minerals, Clays Clay Miner. 28 (1980) 161–172.
[28] D.W. Evans, J.J. Alberts, R.A. Clark III, Reversible ion-exchange fixation of cesium-137 leading to mobilization from reservoir sediments, Geochim. Cosmochim. Acta 47 (1983) 1041–1049.
[29] Q.H. Fan, M. Tanaka, K. Tanaka, A. Sakaguchi, Y. Takahashi, An EXAFS study on the effect of natural organic matter and the expandability of clay minerals on cesium adsorption and mobility, Geochim. Cosmochim. Acta 135 (2014) 49–65.
[30] E. Ferrage, B.A. Sakharov, L.J. Michot, A. Delville, A. Bauer, B. Lanson, S. Grangeon, G. Frapper, M. Jiménez-Ruiz, G.J. Cuello, Hydration properties and

interlayer organization of water and ions in synthetic Na-smectite with tetrahedral layer charge. Part 2. Toward a precise coupling between molecular simulations and diffraction data, J. Phys. Chem. C 115 (2011) 1867–1881.
[31] N. Filipovic-Vincekovic, D. Barisic, N. Masic, S. Lulic, Distribution of fallout radionuclides through soil surface layer, J. Radioan. Nucl. Chem. Ar. 148 (1991) 53–62.
[32] D. Frenkel, B. Smit, Understanding Molecular Simulation, Academic Press, 2002.
[33] A.J. Fuller, S. Shaw, C.L. Peacock, D. Trivedi, J.S. Small, L.G. Abrahamsen, J.T. Burke, Ionic strength and pH dependent multi-site sorption of Cs onto a micaceous aquifer sediment, Appl. Geochem. 40 (2014) 32–42.
[34] A.J. Fuller, S. Shaw, M.B. Ward, S.J. Haigh, J.F.W. Mosselmans, C.L. Peacock, S. Stackhouse, A.J. Dent, D. Trivedi, I.T. Burke, Caesium incorporation and retention in illite interlayers, Appl. Clay Sci. 108 (2015) 128–134.
[35] S. Gaboreau, F. Claret, C. Crouzet, E. Giffaut, C. Tournassat, Caesium uptake by Callovian-Oxfordian clayrock under alkaline perturbation, Appl. Geochem. 27 (2012) 1194–1201.
[36] E.C. Gaucher, C. Tournassat, F.J. Pearson, P. Blanc, C. Crouzet, C. Lerouge, S. Altmann, A robust model for pore-water chemistry of clayrock, Geochim. Cosmochim. Acta 73 (2009) 6470–6487.
[37] A. Gualtieri, Accuracy of XRPD QPA using the combined Rietveld-RIR method, J. Appl. Cryst. 33 (2000) 267–278.
[38] K.F. Hayes, J.O. Leckie, Modeling ionic strength effects on cation adsorption at hydrous oxide/solution interfaces, J. Colloid Interface Sci. 115 (1987) 564–572.
[39] T. Hiemstra, W.H. Van Riemsdijk, A surface structural approach to ion adsorption: the charge distribution (CD) model, J. Colloid Interface Sci. 179 (1996) 488–508.
[40] T. Hinton, D. Kaplan, A. Knox, D. Coughlin, R. Nascimento, S. Watson, D. Fletcher, B.-J. Koo, Use of illite clay for in situ remediation of ^{137}Cs-contaminated water bodies: field demonstration of reduced biological uptake, Environ. Sci. Technol. 40 (2006) 4500–4505, http://dx.doi.org/10.1021/es060124x.
[41] M. Holmboe, I.C. Bourg, Molecular dynamics simulations of water and sodium diffusion in smectite interlayer nanopores as a function of pore size and temperature, J. Phys. Chem. C 118 (2014) 1001–1013.
[42] M. Honda, I. Shimoyama, Y. Okamoto, Y. Baba, S. Suzuki, T. Yaita, X-ray absorption fine structure at the cesium L_3 absorption edge for cesium sorbed in clay minerals, J. Phys. Chem. C 120 (2016) 5534–5538.
[43] Y.-W. Hsiao, M. Hedström, Molecular dynamics simulations of NaCl permeation in bihydrated montmorillonite interlayer nanopores, J. Phys. Chem. C 119 (2015) 17352–17361.
[44] T. Ikeda, S. Suzuki, T. Yaita, Characterization of adsorbed alkali metal ions in 2:1 type clay minerals from first-principles metadynamics, J. Phys. Chem. A 119 (2015) 8369–8375.
[45] O. Karnland, S. Olsson, U. Nilsson, P. Sellin, Experimentally determined swelling pressures and geochemical interactions of compacted Wyoming bentonite with highly alkaline solutions, Phys. Chem. Earth 32 (2007) 275–286.
[46] Y. Kim, R.J. Kirkpatrick, NMR T_1 relaxation study of ^{133}Cs and ^{23}Na adsorbed on illite, Am. Miner. 83 (1998) 661–665.
[47] T. Kogure, K. Morimoto, K. Tamura, H. Sato, A. Yamagishi, XRD and HRTEM evidence for fixation of cesium ions in vermiculite clay, Chem. Lett. 41 (2012) 380–382.
[48] D.A. Kulik, V.L. Vinograd, N. Paulsen, B. Winkler, (Ca, Sr)CO_3 aqueous-solid solution systems: from atomistic simulations to thermodynamic modeling, Phys. Chem. Earth 35 (2010) 217–232.
[49] K.D. Kwon, A.G. Newton, Structure and stability of pyrophyllite edge surfaces: effect of temperature and water chemical potential, Geochim. Cosmochim. Acta 190 (2016) 100–114.
[50] L.P. Lavikainen, J.T. Hirvi, S. Kasa, T. Schatz, T.A. Pakkanen, Stability of dioctahedral 2:1 phyllosilicate edge structures based on pyrophyllite models, Theor. Chem. Acc. 134 (2015) 112.
[51] S.S. Lee, P. Fenter, C. Park, N.C. Sturchio, K.L. Nagy, Hydrated cation speciation at the muscovite (001)-water interface, Langmuir 26 (2010) 16647–16651.
[52] S.S. Lee, P. Fenter, K.L. Nagy, N.C. Sturchio, Monovalent ion adsorption at the muscovite (001)-solution interface: relationships among ion coverage and speciation, interfacial water structure, and substrate relaxation, Langmuir 28 (2012) 8637–8650.
[53] C. Liu, J.M. Zachara, S.C. Smith, J.P. McKinley, C.C. Ainsworth, Desorption kinetics of radiocesium from subsurface sediments at Hanford Site, USA, Geochim. Cosmochim. Acta 67 (2003) 2893–2912.
[54] C. Liu, J.M. Zachara, S.C. Smith, A cation exchange model to describe Cs^+ sorption at high ionic strength in subsurface sediments at Hanford site, USA, J. Contam. Hydrol. 68 (2004) 217–238.
[55] X. Liu, J. Chen, M. Sprik, X. Lu, R. Wang, Surface acidity of 2:1-type dioctahedral clay minerals from first principles molecular dynamics simulations, Geochim. Cosmochim. Acta 140 (2014) 410–417.
[56] Y. Marcus, Thermodynamics of solvation of ions. Part 5. Gibbs free energy of hydration at 298.15 K, J. Chem. Soc., Faraday Trans. 87 (1991) 2995–2999.
[57] V. Marry, B. Rotenberg, P. Turq, Structure and dynamics of water at a clay surface from molecular dynamics simulation, Phys. Chem. Chem. Phys. 10 (2008) 4802–4813.
[58] V. Marry, E. Dubois, N. Malikova, S. Durand-Vidal, S. Longeville, J. Breu, Water dynamics in hectorite clays: influence of temperature studied by coupling neutron spin echo and molecular dynamics, Environ. Sci. Technol. 45 (2011) 2850–2855.
[59] D.M.S. Martins, M. Molinari, M.A. Gonçalves, J.P. Mirão, S.C. Parker, Toward modeling clay mineral nanoparticles: the edge surfaces of pyrophyllite and their interaction with water, J. Phys. Chem. C 118 (2014) 26317–27308.
[60] C. McCombie, Nuclear waste management worldwide, Phys. Today 50 (1997) 56–62.
[61] J.P. McKinley, C.J. Zeissler, J.M. Zachara, R.J. Serne, R.M. Lindstrom, H.T. Schaef, R.D. Orr, Distribution and retention of ^{137}Cs in sediments at the Hanford Site, Washington, Environ. Sci. Technol. 35 (2001) 3433–3441.
[62] J.P. McKinley, J.M. Zachara, S.M. Heald, A. Dohnalkova, M.G. Newville, S.R. Sutton, Microscale distribution of cesium sorbed to biotite and muscovite, Environ. Sci. Technol. 38 (2004) 1017–1023.
[63] H. Mukai, T. Hatta, H. Kitazawa, H. Yamada, T. Yaita, T. Kogure, Speciation of radioactive soil particles in the Fukushima contaminated area by IP autoradiography and microanalyses, Environ. Sci. Technol. 48 (2014) 13053–13059.
[64] M. Nakano, K. Kawamura, Y. Ichikawa, Local structural information of Cs in smectite hydrates by means of an EXAFS study and molecular dynamics simulations, Appl. Clay Sci. 23 (2003) 15–23.
[65] A. Nakao, S. Ogasawara, O. Sano, T. Ito, J. Yanai, Radiocesium sorption in relation to clay mineralogy of paddy soils in Fukushima, Japan, Sci. Tot. Environ. 468–469 (2014) 523–529.
[66] A.G. Newton, G. Sposito, Molecular dynamics simulations of pyrophyllite edge surfaces: structure, surface energies, and solvent accessibility, Clays Clay Miner. 63 (2015) 278–290.
[67] A.G. Newton, K.D. Kwon, D.-K. Cheong, Edge structure of montmorillonite from atomistic simulations, Minerals 6 (2016) 25.
[68] M. Okumura, H. Nakamura, M. Machida, Mechanism of strong affinity of clay minerals to radioactive cesium: first-principles calculation study for adsorption of cesium at frayed edge sites in muscovite, J. Phys. Soc. Jpn. 82 (2013) 033802.
[69] T. Okumura, K. Tamura, E. Fujii, H. Yamada, T. Kogure, Direct observation of cesium at the interlayer region in phlogopite mica, Microscopy 63 (1) (2014) 65–72, http://dx.doi.org/10.1093/jmicro/dft045.
[70] C.R. Olsen, P.D. Lowry, S.Y. Lee, I.L. Larsen, N.H. Cutshall, Geochemical and environmental processes affecting radionuclide migration from a formerly used seepage trench, Geochim. Cosmochim. Acta 50 (1986) 593–607.
[71] S. Pacala, R. Socolow, Stabilization wedges: solving the climate problem for the next 50 years with current technologies, Science 305 (2004) 968–972.
[72] Pestana L.R., Kolluri K., Head-Gordon T., Lammers L, Direct exchange mechanism for interlayer ions in non-swelling clays (in review).
[73] S. Plimpton, Fast parallel algorithms for short-range molecular dynamics, J. Comput. Phys. 117 (1995) 1–42.
[74] C. Poinssot, B. Baeyens, M.H. Bradbury, Experimental and modelling studies of caesium sorption on illite, Geochim. Cosmochim. Acta 63 (1999) 3217–3227.
[75] M. Predota, Z. Zhang, P. Fenter, D.J. Wesolowski, P.T. Cummings, Electric double layer at the rutile (110) surface. 2. Adsorption of ions from molecular dynamics and X-ray experiments, J. Phys. Chem. B 108 (2004) 12061–12072.
[76] P. Rajec, V. Sucha, D.D. Eberl, J. Srodon, F. Elsass, Effect of illite particle shape on cesium sorption, Clays Clay Miner. 47 (1999) 755–760.
[77] M.K. Ridley, T. Hiemstra, W.H. van Riemsdijk, Machesky, Inner-sphere complexation of cations at the rutile-water interface: a concise surface structural interpretation with the CD and MUSIC model, Geochim. Cosmochim. Acta 73 (2009) 1841–1856.
[78] B. Rotenberg, V. Marry, R. Vuilleumier, N. Malikova, C. Simon, P. Turq, Water and ions in clays: unraveling the interlayer/micropore exchange using molecular dynamics, Geochim. Cosmochim. Acta 71 (2007) 5089–5101.
[79] B. Rotenberg, J.-P. Morel, V. Marry, P. Turq, N. Morel-Desrosiers, On the driving force of cation exchange in clays: insights from combined microcalorimetry experiments and molecular simulation, Geochim. Cosmochim. Acta 73 (2009) 4034–4044.
[80] J.-P. Ryckaert, G. Ciccotti, H.J.C. Berendsen, Numerical integration of the cartesian equations of motion of a system with constraints: molecular dynamics of n-alkanes, J. Comput. Phys. 23 (1977) 327.
[81] C.I. Sainz-Díaz, J. Cuadros, A. Hernández-Laguna, Analysis of cation distribution in the octahedral sheet of dioctahedral 2:1 phyllosilicates by using inverse Monte Carlo methods, Phys. Chem. Miner. 28 (2001) 445–454.
[82] H. Sakuma, K. Kawamura, Structure and dynamics of water on Li^+-, Na^+-, K^+-, Cs^+-, H_3O^+-exchanged muscovite surfaces: a molecular dynamics study, Geochim. Cosmochim. Acta 75 (2011) 63–81.
[83] B.L. Sawhney, Selective sorption and fixation of cations by clay minerals: a review, Clays Clay Miner. 20 (1972) 93–100.
[84] S. Shiozawa, Vertical migration of radiocesium in soil in Fukushima, in: Agricultural Implications of the Fukushima Nuclear Accident, 2014. http://dx.doi.org/10.1007/978-4-431-54328-2_6.
[85] A.A. Skelton, P. Fenter, J.D. Kubicki, D.J. Wesolowski, P.T. Cummings, Simulations of the quartz ($10\bar{1}1$)/water interface: a comparison of classical force fields, ab initio molecular dynamics, and X-ray reflectivity experiments, J. Phys. Chem. C 115 (2011) 2076–2088.
[86] P.G. Slade, J.P. Quirk, K. Norrish, Crystalline swelling of smectite samples in concentrated NaCl solutions in relation to layer charge, Clays Clay Miner. 39 (1991) 234–238.
[87] J.T. Smith, R.N.J. Comans, Modelling the diffusive transport and remobilisation of ^{137}Cs in sediments: the effects of sorption kinetics and reversibility, Geochim. Cosmochim. Acta 60 (1996) 995–1004.

[88] D.E. Smith, L.X. Dang, Computer simulations of NaCl association in polarizable water, J. Chem. Phys. 100 (1994) 3757–3766.
[89] G. Sposito, The Surface Chemistry of Natural Particles, Oxford University Press, 2004.
[90] S. Staunton, M. Roubaud, Adsorption of ^{137}Cs on montmorillonite and illite: effect of charge compensating cation, ionic strength, concentration of Cs, K and fulvic acid, Clays Clay Miner. 45 (1997) 251–260.
[91] C.I. Steefel, S. Carroll, P. Zhao, S. Roberts, Cesium migration in Hanford sediment: a multisite cation exchange model based on laboratory transport experiments, J. Contam. Hydrol. 67 (2003) 219–246.
[92] T.P. Straatsma, H.J.C. Berendsen, J.P.M. Postma, Free energy of hydrophobic hydration: a molecular dynamics study of noble gases in water, J. Chem. Phys. 85 (1986) 6720–6727.
[93] S. Suehara, H. Yamada, Cesium stability in a typical mica structure in dry and wet environments from first-principles, Geochim. Cosmochim. Acta 109 (2013) 62–73.
[94] Y. Tachi, K. Yotsuji, Y. Seida, M. Yui, Diffusion and sorption of Cs^+, I^- and HTO in samples of the argillaceous Wakkanai Formation from the Horonobe URL, Japan: clay-based modeling approach, Geochim. Cosmochim. Acta 75 (2011) 6742–6759.
[95] K. Tamura, T. Kogure, Y. Watanabe, C. Nagai, H. Yamada, Uptake of cesium and strontium ions by artificially altered phlogopite, Environ. Sci. Technol. 48 (2014) 5808–5815.
[96] T. Tamura, Cesium sorption reactions as indicator of clay mineral structures, Clays Clay Miner. 10 (1961) 389–398.
[97] B.J. Teppen, D.M. Miller, Hydration energy determines isovalent cation exchange selectivity by clay minerals, Soil Sci. Soc. Am. J. 70 (2006) 31–40.
[98] C. Tournassat, E. Ferrage, C. Poinsignon, L. Charlet, The titration of clay minerals II. Structure-based model and implications for clay reactivity, J. Colloid Interface Sci. 273 (2004) 234–246.
[99] C. Tournassat, I.C. Bourg, M. Holmboe, G. Sposito, C.I. Steefel, Molecular dynamics simulations of anion exclusion in clay interlayer nanopores, Clays Clay Miner. 64 (2016) 374–388.
[100] N.B. Turner, J.N. Ryan, J.E. Saiers, Effect of desorption kinetics on colloid-facilitated transport of contaminants: cesium, strontium, and illite colloids, Water Resour. Res. 42 (2006) W12S09.
[101] A.P. Vanselow, Equilibria of the base-exchange reactions of bentonites, permutites, soil colloids, and zeolites, Soil Sci. 33 (1932) 95–113.
[102] J.M. Wampler, E.J. Krogstad, W.C. Elliott, B. Kahn, D.I. Kaplan, Long-term selective retention of natural Cs and Rb by highly weathered coastal plain soils, Environ. Sci. Technol. 46 (2012) 3837–3843.
[103] G.N. White, L.W. Zelazny, Analysis and implications of the edge structure of dioctahedral phyllosilicates, Clays Clay Miner. 36 (1988) 141–146.
[104] T. Yasunari, A. Stohl, R. Hayano, J. Burkhart, S. Eckhardt, T. Yasunari, Cesium-137 deposition and contamination of Japanese soils due to the Fukushima nuclear accident, Proc. Natl. Acad. Sci. 108 (2011) 49, http://dx.doi.org/10.1073/pnas.1112058108.
[105] N. Yoshida, J. Kanda, Tracking the Fukushima radionuclides, Science 336 (2012) 1115, http://dx.doi.org/10.1126/science.1219493.
[106] J.M. Zachara, S.C. Smith, C. Liu, J.P. McKinley, R.J. Serne, P.L. Gassman, Sorption of Cs^+ to micaceous subsurface sediments from the Hanford site, USA, Geochim. Cosmochim. Acta 66 (2002) 193–211.
[107] L.K. Zaunbrecher, R.T. Cygan, W.C. Elliott, Molecular models of cesium and rubidium adsorption on weathered micaceous minerals, J. Phys. Chem. A 119 (2015) 5691–5700.

Electronic Annex

Density functional theory (DFT) methods. We evaluated the electronic structure of a muscovite (110)-edge using DFT-based calculations performed in the Vienna Ab initio Simulation Package (VASP; Kresse and Hafner, 1993, 1994; Kresse and Furthmüller, 1996), which supports the projector augmented wave (PAW; Kresse and Joubert, 1999) and generalized gradient approximations (GGA), among others. We use BLYP functional (Becke, 1988; Lee et al., 1988) with Grimm's van der Waals correction (Grimme et al., 2010). The cut-off energies in structural relaxation calculations are set to be 600 eV and 5×1×3 k-point grids are taken in the relaxation. In all the calculations, the structural relaxation is repeated until all the forces on all atoms are below 0.02 eV/ Å. All the DFT calculations are executed the SGI ICE X supercomputer at the Japan Atomic Energy Agency.

We constructed a periodically replicated (110)-type edge structure for muscovite, with edges separated by 10 Å of vacuum (Figure EA1). The lattice constants of the unit cell are provided in Table EA1. Charge density is evaluated for comparison with the Oe6- and Oe3-Al chemical bonds. The charge density in the vicinity of Al, Oe3, and Oe6 atomic positions are shown in Figures EA2. The maximum electron density is 0.04 /Å^3 in these figures. Figure EA2c clearly shows a significant break in electron density in the Al-Oe3 bond.

Thermodynamic integration (TI) calculation methods. For our TI calculations, the size (σ_i) and well-depth (ε_i) parameters describing the Van der Waals interaction energy ϕ between two ions of type *i* on the Lennard-Jones 6-12 interaction model [$\phi(r_i) = 4\ \varepsilon_i\ [(\sigma_i/r_i)^{12} - (\sigma_i/r_i)^6]$ were modified from the value for K to the value for Na or Cs were

modified in a series of small steps. More precisely, we chose a thermodynamic path in which $\sigma(\lambda) = (1-\lambda) \times \sigma_K + \lambda \times \sigma_{final}$ (with $\sigma_{final} = \sigma_{Na}$ or σ_{Cs}) and λ was incremented in 15 (K to Cs) or 25 (K to Na) regular steps. The parameter ε_i was not varied, because $\varepsilon_{Na} = \varepsilon_K = \varepsilon_{Cs}$ according to the Smith-Dang parameters for Na, K, Cs, and Cl (Smith and Dang, 1994; Dang, 1995). Each small transformation step was followed by 2.5 ns of equilibration and 1.5 ns of simulation in the NPT ensemble. At each λ-value, 350 (for the ions in water) or 1100 to 1500 snapshots (for the ions on the clay surface) of the coordination of the ions of interest were used to calculate the ensemble average value of $\langle \partial \mathcal{H} / \partial \lambda \rangle_\lambda$, where $\mathcal{H}$ is the Hamiltonian. Finally, the Gibbs free energy difference for the transformation of K to Na or Cs was calculated as $\Delta G = \int_0^1 \langle \partial \mathcal{H} / \partial \lambda \rangle_\lambda \, \mathrm{d}\lambda$.

Table EA1. Lattice constants of the (110)-edge system.

a (Å)	b (Å)	c (Å)	α (degrees)	β (degrees)	γ (degrees)
5.220	23.9759	10.2837	80.3973	95.8120	90.0791

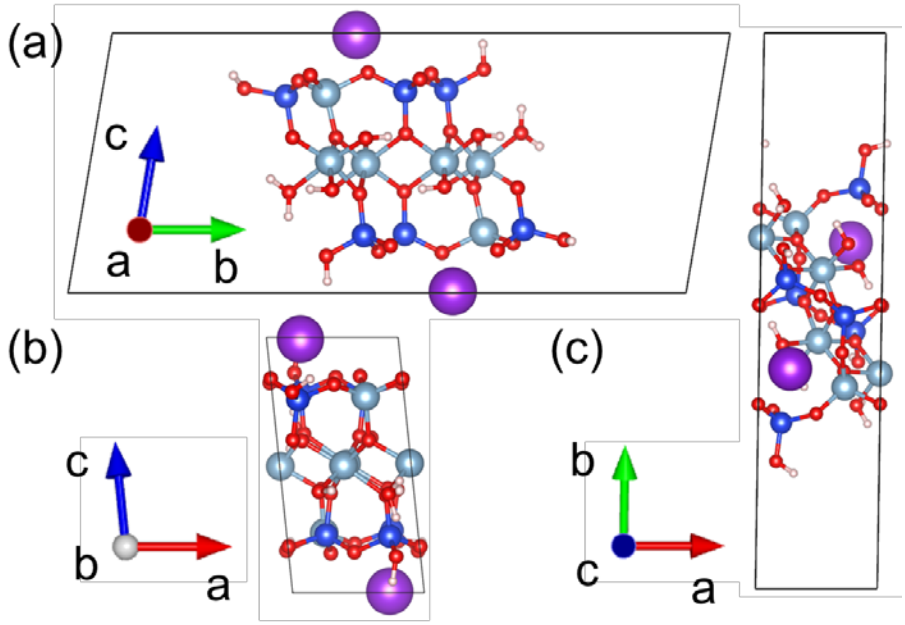

Figure EA1. Illustration of the (110)-edge structure of muscovite. Purple, silver, blue, red, and pink spheres represent potassium, aluminum, silicon, oxygen, and hydrogen atoms. Projected figure on (a) b-c (b) c-a and (c) a-b planes are shown. The width of the vacuum space in the b-axis direction is 10Å. The lattice parameters are shown in Table EA1.

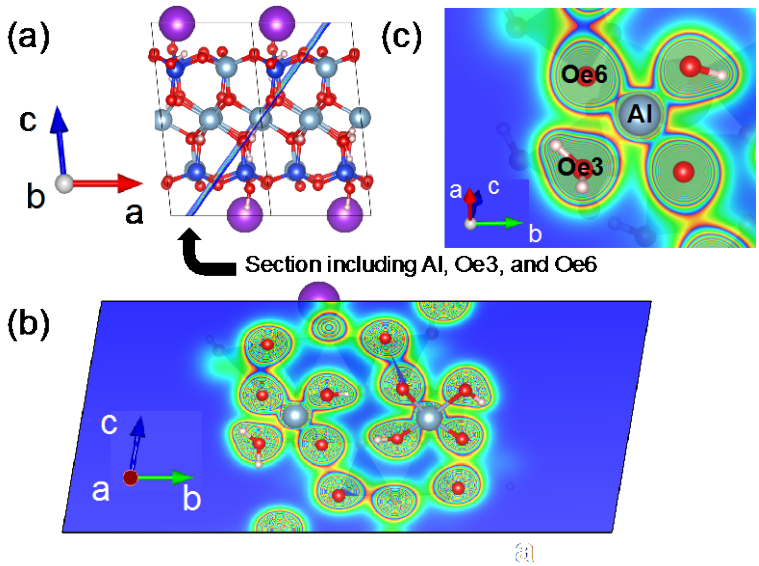

Figure EA2. Cross section (a) of the electron density distribution surrounding Al, Oe3, and Oe6 (b), with a maximum electron density of is 0.04 $Å^{-3}$. The electron density minimum separating doubly protonated Oe3 is shown in greater detail in (c).

Table EA2. Specific surface excess of Cs and Na on basal and edge sites, with 2 s.e. uncertainties. Edge H- and I- site surface excess values are normalized to the total edge area and basal values are normalized to the basal surface area. Basal surfaces and edge H-sites accommodate the majority of cation sorption to illite exterior surfaces. Adsorption in the interlayers was not observed on the 50 ns time scale of our MD simulations.

	n^w_{Cs} (μmol m^{-2})				n^w_{Na} (μmol m^{-2})			
x_{Cs}	**basal**	**edge H-site**	**edge I-site**	**whole particle**	**basal**	**edge H-site**	**edge I-site**	**whole particle**
0.1	0.15(3)	0.22(5)	-0.03(2)	0.34(5)	1.69(14)	1.13(17)	0.25(6)	2.91(5)
0.2	0.29(2)	0.57(6)	-0.01(4)	0.69(6)	1.62(12)	0.65(9)	0.05(8)	2.41(4)
0.3	0.44(4)	1.24(9)	0.03(4)	0.95(8)	1.52(11)	0.54(10)	-0.09(7)	2.32(5)
0.4	0.74(5)	0.92(7)	-0.04(4)	1.31(11)	1.10(8)	0.94(7)	0.05(8)	1.86(4)
0.5	0.75(5)	1.39(9)	0.01(9)	1.57(9)	1.26(7)	0.66(7)	-0.09(9)	1.72(7)
0.6	1.17(9)	1.10(19)	-0.32(11)	1.71(10)	0.82(12)	0.76(16)	0.24(6)	1.55(8)
0.7	1.33(6)	1.38(10)	-0.23(11)	1.94(11)	0.70(13)	0.40(7)	0.14(11)	1.16(4)
0.8	1.68(6)	1.43(8)	-0.04(8)	2.61(16)	0.43(8)	0.42(5)	0.016(5)	0.73(3)
0.9	1.78(7)	1.28(20)	0.22(10)	3.04(27)	0.25(5)	0.35(3)	-0.01(5)	0.41(2)
1.0	2.23(6)	1.23(7)	0.05(5)	3.29(13)	0.00(0)	0.00(0)	0.00(0)	0.00(0)

References

Becke, A.D. (1988) Density-functional exchange-energy approximation with correct asymptotic behavior. *Phys. Rev. A* **38**, 3098.

Grimme, S., Antony, J., Ehrlich, S., and Krieg, S. (2010) A consistent and accurate ab initio parametrization of density functional dispersion correction (dft-d) for the 94 elements H-Pu', *J. Chem. Phys.* **132**, 154104.

Kresse, G. and Furthmüller, J. (1996b) Efficient iterative schemes for *ab initio* total-energy calculations using a plane-wave basis set. *Phys. Rev. B* **54**, 11169-11186.

Kresse, G. and Hafner, J. (1993) *Ab initio* molecular-dynamics simulation of the liquid-metal–amorphous-semiconductor transition in germanium. *Phys. Rev. B* **49**, 14251-14269.

Kresse, G. and Hafner, J. (1994) Ab initio molecular dynamics for liquid metals. *Phys. Rev. B* **47**, 558-561.

Kresse, G. and Joubert, D. (1999) From ultrasoft pseudopotentials to the projector augmented-wave method. *Phys. Rev. B* **59**, 1758-1775.

Lee, C., Yang, W. and Parr, R. G. (1988) Development of the Colle-Salvetti correlation-energy formula into a functional of the electron density. *Phys. Rev. B* **37**, 785.